Progress In Electromagnetics Research M, Vol. 37, 191–202, 2014

Microwave Tunable Metasurfaces Implemented with Ferroelectric Materials and Periodical Copper Wires

Li-Hao Yeh and Jean-Fu Kiang*

Abstract—A tunable metasurface composed of multiple resonant units is proposed, with each unit containing a block of $SrTiO_3$ ferroelectric and a periodical copper-wire structure. The local transmission coefficient of the metasurface can be controlled by tuning the permittivity of $SrTiO_3$ via a bias voltage. A tunable metasurface is simulated to steer the beam direction at the angles of 30° and 14.47°, respectively. Another one is simulated to focus the wave beam at the focal lengths of $2\lambda_0$ and $4\lambda_0$, respectively.

1. INTRODUCTION

A metasurface is a thin layer of metamaterial, which displays different properties from those of a three-dimensional metamaterial [1]. Electromagnetic wave can be manipulated using a metasurface much thinner than one wavelength, leading to much lower loss than using three-dimensional metamaterial. The fabrication process of the former is usually less complicated than that of the latter.

Metasurfaces comprised of nanoantenna phased-array have been investigated for holography, quarter-waveplate, metalenses, and meta-mirrors [2–17]. By the Fermat's principle, a phase discontinuity is introduced across the metasurface [2]. By tuning this phase discontinuity, both the reflected wave and the transmitted wave can be steered to other directions than those predicted with the conventional reflection law and Snell's law.

Certain phase gradient on the surface has been achieved using an array of V-antennas with different geometries [2]. An antenna-based hologram has also been proposed using similar V-antennas [3], in which the phase response of a pixel can be chosen among eight discrete levels implemented with eight V-antennas of different geometries, respectively.

Metasurfaces comprised of L-shaped slot-antennas and concentric loop-antennas, respectively, are reported to have the capability of tuning the amplitude and the phase, respectively, of the transmission coefficient [4]. By cascading these two metasurfaces, the phase and amplitude of the incident light can be arbitrarily tuned.

A plasmonic metasurface composed of unit cells, each containing two orthogonal nanoslits, has been designed to respond differently to the incident wave of two orthogonal polarizations [5]. The amplitude response of these two nanoslits are designed to be the same, while the phase response has a difference of $\pi/2$, serving the function of a quarter-wavelength plate. A similar plate has been realized using V-antennas [6], which has a broader bandwidth than that made of nanoslits.

Metasurfaces have also been proposed to implement metalenses working in different bands [7–10]. Near-infrared metalenses and axicons have been proposed at $\lambda \sim 1.5\,\mu$m [7, 8] and 1 THz [10]. In [11], an antenna element has been proposed to generate a local transmittance of $e^{j\phi}$ on a metasurface. Beam steering and focusing can thus be achieved by tuning the phase distribution on the metasurface.

Similarly, meta-mirrors have been made by tuning the phase of the reflected light using nanobricks of different geometries at different locations [12–14]. Flat mirrors can thus be implemented to focus waves [12] and steering [13, 14].

Received 16 June 2014, Accepted 29 July 2014, Scheduled 4 August 2014

* Corresponding author: Jean-Fu Kiang (jfkiang@ntu.edu.tw).
The authors are with the Department of Electrical Engineering, National Taiwan University, Taipei 106, Taiwan.

Metasurfaces can also be designed using the concept of Huygens' surfaces, on which equivalent electric and magnetic surface currents are used to describe the field difference across a metasurface [15–17]. By properly adjusting the electric and the magnetic currents, the reflected field can be significantly reduced, leading to a strong transmittance. Wave steering has been realized at the frequency of 10 GHz [15]. Focusing of waves with circular polarization has been achieved by cascading several Huygens' metasurfaces [16]. In principle, an arbitrary waveplate can be implemented as a Huygens' surface [17].

Electromagnetic tunability for different applications has been implemented with electro-optic crystal [18], liquid crystal [19], and ferroelectric materials [20]. However, fewer discussions have been given to the tunability of metasurfaces.

In this work, we propose an idea to implement a tunable metasurface for beam steering and focusing, using ferroelectric materials with tunable permittivity by voltage. This work is organized as follows: Theories and implementation concepts are briefly reviewed in Section 2, the design of periodical resonant units using ferroelectric block and copper wires is described in Section 3. Demonstrations of beam steering and beam focusing with this type of tunable metasurfaces are presented in Sections 4 and 5, respectively. Finally, some conclusions are drawn in Section 6.

2. THEORIES AND IMPLEMENTATION CONCEPTS

A metasurface for transforming an incident beam can be designed as follows. Firstly, analyze the transmission or reflection response of a periodical array, containing specific type of identical resonant units. Secondly, summarize the response of the above array over a range of parameters of the resonant unit. Thirdly, decompose an array into small regions, each containing a few identical resonant units. The parameters in each region are properly chosen to achieve the desired distribution of response over the whole array. The resonant units are required to have a sufficient range of phase response around their resonant frequencies.

2.1. Tunable Resonance

Plasmonic resonance in a metal-dielectric structure has been widely explored to implement resonant units with a wide range of phase change and a nearly constant amplitude [2–14]. These resonant units are usually much smaller than the operational wavelength.

The plasmonic resonance is determined by the geometry and permittivity of the constituent materials, always involving a negative-permittivity material and a positive-permittivity one. The resonant condition on the interface between two half-space materials is $\epsilon_1 = -\epsilon_2$ [21]. The condition for a spherical nanoparticle is $\epsilon_s = -2\epsilon_e$ [21], where ϵ_s and ϵ_e are the permittivity of the sphere and the ambient environment, respectively.

In [11], a three-layered structure of periodic plasmonic-dielectric nanobricks has been designed for beam steering and focusing. The transmission coefficient with near-constant amplitude and a phase range of 2π can be achieved by varying the width ratio between the two materials within a resonant unit.

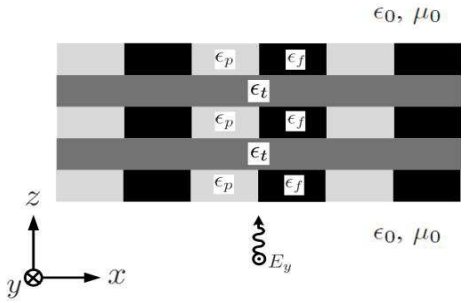

Figure 1. Configuration of a three-layered metasurface.

Figure 1 shows the structure of a three-layered metasurface, satisfying the plasmonic resonant condition, $\epsilon_p = -\epsilon_f$, where ϵ_p and ϵ_f are the permittivity of the plasmonic material and the ferroelectric, respectively. The permittivity of the latter can be tuned by applying a bias voltage up to several hundreds even thousands of volts, at frequency up to 100 GHz [20].

If a single layer of plasmonic/ferroelectric resonant units can not provide a sufficient phase change around the resonant frequency, more layers will be needed. A two-layered and a three-layered metasurfaces will be analyzed respectively. A proper spacing material (with permittivity ϵ_t) between layers is also used to support the structure of the metasurface.

2.2. Transmission Coefficient of Periodical Multilayered Metasurfaces

Firstly, we calculate the transmission coefficient of a periodical metasurface made of identical bricks. For the two-layered metasurface, the transmission coefficients are calculated as a function of ferroelectric permittivities in the first and the second layer, ϵ_{f1} and ϵ_{f2}, respectively. In the three-layered metasurface, the ferroelectric permittivities of the first and the third layers are set the same as $\epsilon_{f\text{out}}$, and that of the second layer is $\epsilon_{f\text{in}}$.

3. DESIGN OF PERIODICAL RESONANT UNITS

3.1. Permittivity of Ferroelectric Material

The permittivity of a ferroelectric material, at frequency up to 100 GHz, can be expressed as [20]

$$\epsilon_{rf} = \frac{\epsilon_{00}}{\left[\sqrt{\xi^2+\delta^3}+\xi\right]^{2/3} + \left[\sqrt{\xi^2+\delta^3}-\xi\right]^{2/3} - \delta + a_f^2} \tag{1}$$

with

$$\xi = \sqrt{\xi_B^2 + \xi_S^2} \tag{2}$$

$$\delta = \left(\frac{\Theta_F}{T_C}\right)\sqrt{\frac{1}{16} + \left(\frac{T}{\Theta_F}\right)^2} - 1 \tag{3}$$

where ϵ_{00} is a constant; $a_f = \sqrt{2\epsilon_{00}/\alpha h}$, h is the thickness of the ferroelectric, and α is related to the lattice oscillation type; $\xi_B = E_b/E_N$, E_b is the biasing electric field, and E_N is a normalization constant; ξ_S is a parameter related to the dispersion effect; Θ_F is the Debye temperature of the sublattice oscillation; T_C is the Curie temperature; T is the temperature of the ferroelectric.

$SrTiO_3$ is a commonly used ferroelectric at microwave frequencies [20, 22, 23]. In this work, the parameters of $SrTiO_3$ are chosen to be $T_C = 42\,\text{K}$, $\Theta_F = 175\,\text{K}$, $\xi_S = 0.018$, $\epsilon_{00} = 2081$, $E_N = 19.3\,\text{kV/cm}$, $\alpha = 2 \times 10^9\,\text{m}^{-1}$ [20].

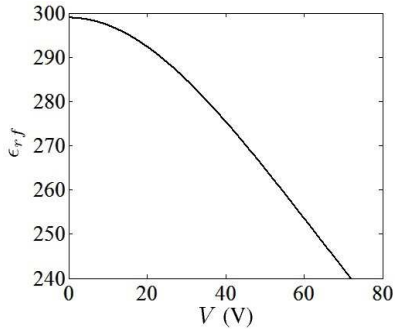

Figure 2. Permittivity of $SrTiO_3$ layer with thickness $h = 2.8\,\mu\text{m}$, under a biasing voltage.

Figure 2 shows the permittivity of a $SrTiO_3$ layer as a function of the biasing voltage. Its thickness is $h = 2.8\,\mu m$, and the room temperature is $T = 300\,K$. The imaginary part of the permittivity is neglected since the loss tangent of the $SrTiO_3$ is very small ($\sim 10^{-4}$).

3.2. Effective Permittivity of Periodical Metal Wires

The plasma frequency of a bulk metal falls in the optical band. A periodical metal-wire structure of simple cubic form can have its plasma frequency in the microwave band, and its permittivity can be modeled as [24]

$$\epsilon_{rp} = 1 - \frac{\omega_p^2}{\omega(\omega - j\epsilon_0 a^2 \omega_p^2 / \pi r^2 \sigma)} \tag{4}$$

where a is the lattice constant of the simple cubic structure; r and σ are the radius and the conductivity, respectively, of the metal wires; and

$$\omega_p = \sqrt{\frac{2\pi c^2}{a^2 \ln(a/r)}} \tag{5}$$

is the plasma frequency. It is assumed that thin metal wires are widely spaced ($\ln(a/r) > 1$) and a is much shorter than the operating wavelength [24].

Figure 3 shows the permittivity of the periodic copper-wire structure. The effective permittivity at 5.8 GHz is $\epsilon_{rp} = -263.4 - j0.1421$, which has the same order of magnitude as that of $SrTiO_3$ (240∼300).

3.3. Two-Dimensional Problems

Consider a special case in which the field components are independent of y, and a plane wave of TE polarization ($\bar{E} = \hat{y}E_y$) is normally incident from the $-z$ direction. A two-dimensional frequency-domain finite-difference (2D-FDFD) technique is applied to calculate the transmission coefficient of the periodical multilayered metasurface, with various layer length (ℓ) and spacing (d) between layers. The total width of a resonant unit is chosen to be $w = \lambda_0/8 = 6.5\,mm$. Figure 4 shows the computational domain of the structure over one period in the x direction, where periodical boundary condition is imposed on the two dashed lines.

The thickness of $SrTiO_3$ in the y direction, as shown in Figure 2, is chosen to be $h = 2.8\,\mu m$. The permittivity curve in Figure 2 can be applied, with the range of biasing voltage below 100 V. An

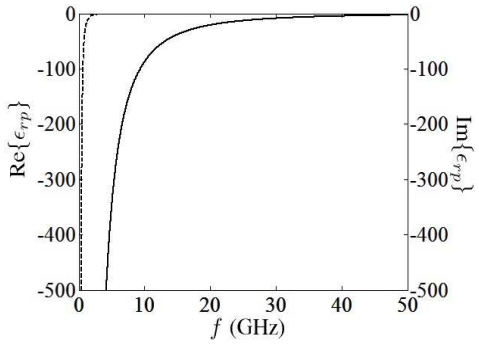

Figure 3. Permittivity of periodic copper-wire structure, $\sigma = 5.8 \times 10^7\,S/m$, $a = 0.68\,mm$ and $r = 0.02\,mm$. ——: Re$\{\epsilon_{rp}\}$, − − −: Im$\{\epsilon_{rp}\}$.

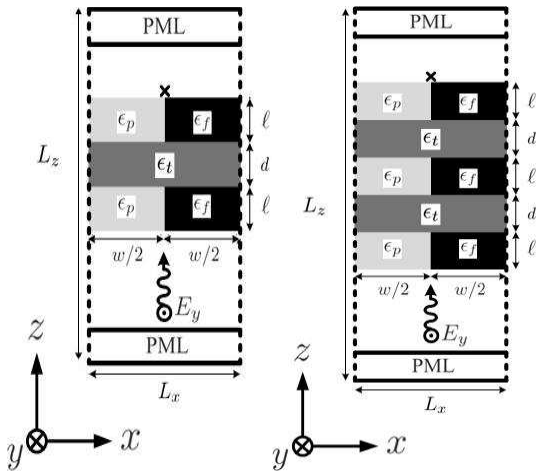

Figure 4. Computational domain of (a) two-layered metasurface and (b) three-layered metasurface. Periodic boundary condition is imposed on two dashed lines.

insulation material, TiO_2, is inserted between two segments of $SrTiO_3$ in the y direction. The TiO_2 can withstand a 70 V potential difference over a separation of $s = 0.4\,\mu m$ [25]. The permittivity of TiO_2 in the microwave band is $\epsilon_{ins} = 139.6\epsilon_0$ [20, 26], hence the effect of permittivity discontinuity between ferroelectric and insulator can be neglected.

Figure 5 shows the cross section, in the xy plane, of one resonant unit. The wavelengths inside the ferroelectric ($\epsilon_{rf} \simeq 250$) and the TiO_2 are 3.29 mm and 4.4 mm, respectively; both are much larger than the separation ($s = 0.4\,\mu m$). Hence, the effect of the insulator on the wave behavior in the y direction can be reasonably neglected in the simulation.

3.4. Determination of Layer Length

As shown in Figure 4, perfect matching layers (PML's) are applied above and below the computational domain. The size of the computational domain is $L_x \times L_z = 6.5 \times 100\,mm^2$, which is divided into 50×400 Yee's cells, with the size of each Yee's cell being $\Delta x \times \Delta z = 0.13 \times 0.25\,mm^2$.

Next, we search for a proper layer length (ℓ) to acquire a wide range of phase variation and moderate amplitude variation when ϵ_{rf} is varied. Figure 6 shows the amplitude and phase of the transmission coefficient of a single layer of bricks when ℓ and ϵ_{rf} are varied. Four usable layer lengths are observed at $\ell = 2$, 3.75, 5.5 and 7.25 mm, around which the phase variation is wide and the amplitude variation is moderate. In the subsequent simulations, we choose $\ell = 2\,mm$. As ϵ_{rf} is varied from 240 to 300, the phase changes by about 180°, but the amplitude is far from constant.

3.5. Determination of Spacing between Layers

The spacing (d) between layers strongly affects the transmission coefficient. Teflon (PTFE) is chosen as the spacer for its low loss and high breakdown voltage [20], with permittivity of $\epsilon_{rt} = 2.01 - j0.005$ at 5.8 GHz [27].

Figure 7 shows the amplitude of transmission coefficient at various spacing (d). In both configurations, the amplitude is roughly constant when $d \geq 5.5\,mm$. Hence, we choose $d = 5.5\,mm$ in the subsequent simulations.

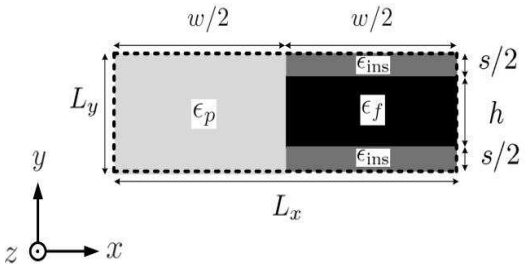

Figure 5. Cross section (in xy plane) of one resonant unit.

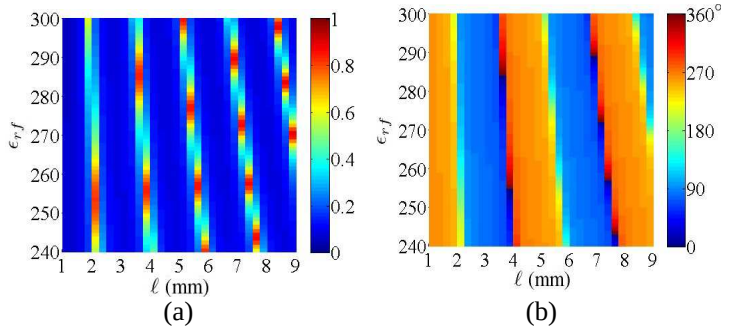

Figure 6. (a) Amplitude and (b) phase of the transmission coefficient as a function of layer length (ℓ) and ϵ_{rf}.

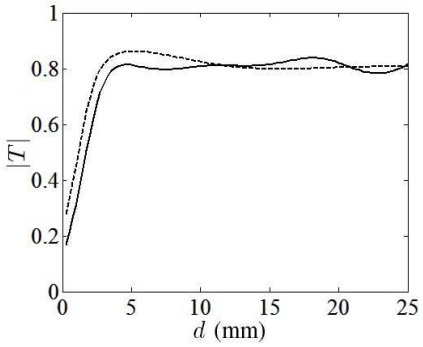

Figure 7. Amplitude of transmission coefficient as a function of spacing (d). $\epsilon_{rf} = 252$, $\ell = 2\,\text{mm}$; $- - -$: two-layered metasurface, ———: three-layered metasurface.

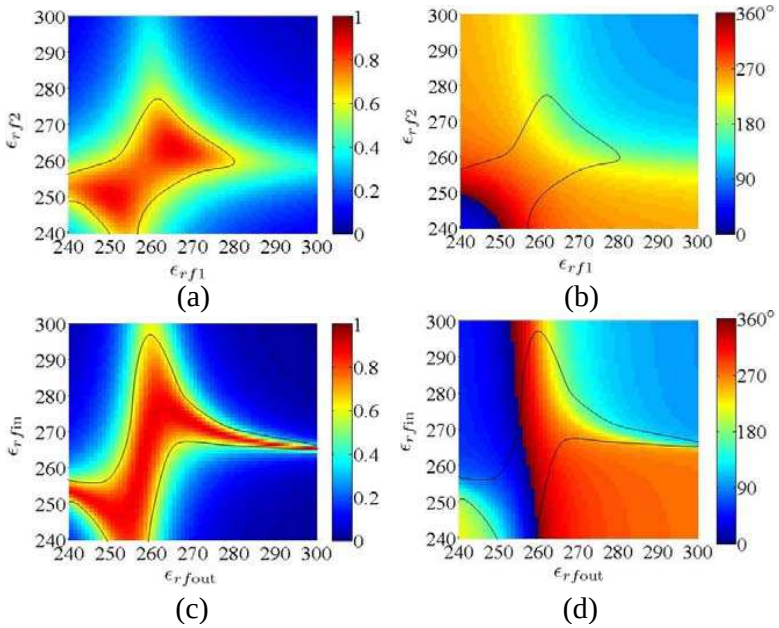

Figure 8. (a) Amplitude and (b) phase of transmission coefficient of the two-layered metasurface; (c) amplitude and (d) phase of transmission coefficient of the three-layered metasurface; $d = 5.5\,\text{mm}$ and $\ell = 2\,\text{mm}$. The black contour encircles the region with amplitude larger than 0.6.

3.6. Available Phase Range

The tunable metasurface is required to provide a phase range of more than 360°, with nearly constant amplitude. Figure 8 shows how the transmission coefficient varies with the ferroelectric permittivities in different layers. For the two-layered metasurface (Figures 8(a) and 8(b)), resonance occurs when both ϵ_{f1} and ϵ_{f2} are close to 250 or 270. The phase changes by about 180° around each resonant region, leading to a total phase change of about 360°. However, the amplitude is not nearly constant in the same regions. To look in another way, the black contour in Figures 8(a) and 8(b) encircles the region with amplitude of transmission coefficient greater than 0.6, and the phase variation within this region is less than 360°.

On the other hand, the three-layered metasurface (Figures 8(c) and 8(d)) can provide a region with relatively constant amplitude and a phase change of about 360°. Thus, the latter will be used for beam steering and focusing, respectively, in the next two sections.

4. METASURFACE FOR BEAM STEERING

By applying the Fermat's principle to analyze the optical path difference across the interface of two media with a phase discontinuity, the Snell's law and the reflection law can be generalized as [2]

$$\begin{aligned} n_t \sin\theta_t - n_i \sin\theta_i &= -\frac{\lambda_0}{2\pi}\frac{d\Phi}{dx} \\ \sin\theta_r - \sin\theta_i &= -\frac{\lambda_0}{2\pi n_i}\frac{d\Phi}{dx} \end{aligned} \tag{6}$$

where n_i and n_t are the refractive indices of the medium on the incident side and the transmitted side, respectively; θ_i, θ_r and θ_t are the incident angle, the reflected angle and the transmitted angle, respectively; λ_0 is the wavelength in free space; Φ is the phase discontinuity across the interface due to the metasurface. Eq. (6) can be rewritten over a two-dimensional interface as

$$\begin{aligned} \bar{k}_{is} - \nabla_s\Phi &= \bar{k}_{ts} \\ \bar{k}_{is} - \nabla_s\Phi &= \bar{k}_{rs} \end{aligned} \tag{7}$$

where $\bar{k}_{is}$, $\bar{k}_{rs}$ and $\bar{k}_{ts}$ are the wavenumber vectors of the incident wave, the reflected wave and the transmitted wave, respectively, projected onto the interface; ∇_s is the 2D gradient operator on the interface. By tuning the phase discontinuity on the surface, both the reflected wave and the transmitted wave can be steered toward other directions than those predicted by the conventional reflection law and Snell's law.

Next, we will design a three-layered metasurface to steer a normally incident TE wave toward a specific direction. Consider the intended steering angles of $\theta_t = 30°$ and $\theta_t = 14.47°$, corresponding to phase gradients of $d\Phi/dx = -\pi/\lambda_0$ and $d\Phi/dx = -\pi/2\lambda_0$, respectively; and a linear phase variation of 2π can be acquired along the x direction over a distance of $2\lambda_0$ and $4\lambda_0$, respectively.

The width of a single resonant unit is chosen to be $\lambda_0/8$. To realize a linear phase change of 2π over $2\lambda_0$ along the x direction, we group 16 resonant units into 8 pairs, with each pair comprised of

Table 1. Permittivities for beam steering toward 30°.

No.	1	2	3	4	5	6	7	8
ϵ_{rfout}	257	260	264	267	274	245	250	255
ϵ_{rfin}	259	266	271	274	271	250	249	248
$\lvert T\rvert$	0.8769	0.8423	0.8154	0.8799	0.7965	0.8601	0.8643	0.8739
$\measuredangle T$	0.2282°	315.1°	270.1°	225.3°	180.5°	133.4°	90.97°	45.47°

Table 2. Permittivities for beam steering toward 14.47°.

No.	1	2	3	4	5	6	7	8
ϵ_{rfout}	257	258	260	261	264	265	267	267
ϵ_{rfin}	259	265	266	271	271	274	274	277
$\lvert T\rvert$	0.8769	0.8776	0.8423	0.8624	0.8154	0.8756	0.8799	0.7892
$\measuredangle T$	0.2282°	337.5°	315.1°	293.6°	270.1°	246.4°	225.3°	201.7°
No.	9	10	11	12	13	14	15	16
ϵ_{rfout}	274	244	245	243	250	253	255	255
ϵ_{rfin}	271	249	250	253	249	248	248	258
$\lvert T\rvert$	0.7965	0.7601	0.8601	0.8278	0.8643	0.8747	0.8739	0.836
$\measuredangle T$	180.5°	157.5°	133.4°	112.8°	90.97°	67.01°	45.47°	22.55°

two identical resonant units adjacent to each other. The phase difference between each pair and its neighboring pair is $-\pi/4$, leading to $d\Phi/dx = -\pi/\lambda_0$ and the steering angle of 30°.

Similarly, to realize a linear phase change of 2π over $4\lambda_0$ along the x direction, the phase difference of $-\pi/8$ between adjacent pairs is required to achieve $d\Phi/dx = -\pi/2\lambda_0$, achieving a steering angle of 14.47°. The permittivities required to steer the beam toward 30° and 14.47°, are retrieved from Figures 8(c) and 8(d), and are listed in Tables 1 and 2, respectively.

Figure 9 shows the distribution of E_y, with a uniform plane wave incident from below the metasurface. The finite-difference time-domain (FDTD) technique is applied, with the periodic boundary condition imposed at $x = \pm 2\lambda_0$. By Huygen's principle, the radiation from all the resonant units form a tilted wavefront moving towards the steering direction.

In order to keep the steered beam from divergence before reaching the target area, a larger aperture is required. Consider an aperture of length $60\lambda_0$ along the x axis, with the same incident plane wave as shown in Figure 9. The field distribution over this large aperture will be 15 repetitions of that in Figure 9. The far field pattern can then be derived by taking the Fourier transform of the aperture field distribution along the line at $z = 2\lambda_0$.

Figure 10 shows the far field pattern derived by applying the near-to-far transformation to the near field distribution over the aperture [28]. The near field over the leftmost and rightmost $4\lambda_0$ over the aperture are linearly tapered to reduce the side lobes of the far field pattern.

The $60\lambda_0$-wide aperture is a periodic structure, which explains the appearance of grating lobes in Figure 10. The periods in the x direction of the metasurface used to generate the field patterns in Figures 10(a) and 10(b) are $\Lambda = 2\lambda_0$ and $4\lambda_0$, respectively. The relation between the incident angle and the transmitted angle of the mth Floquet mode is [29]

$$n_t \sin\theta_t = n_i \sin\theta_i + \frac{m\lambda_0}{\Lambda} \tag{8}$$

where Λ is the period on the aperture. The gradient of phase discontinuity on the metasurfaces is

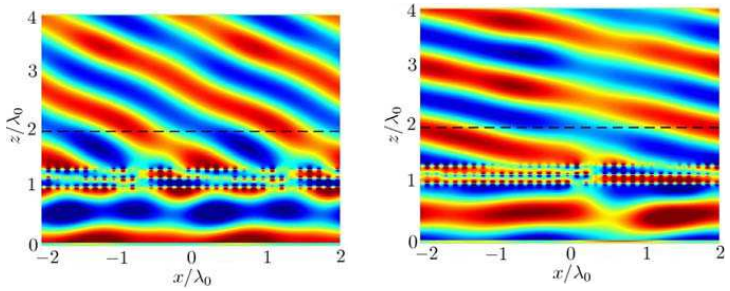

Figure 9. Distribution of E_y simulated by using the FDTD technique, with the steering angle of (a) 30° and (b) 14.47°. The metasurface (with $\ell = 2\,\text{mm}$ and $d = 5.5\,\text{mm}$) is placed at $z = \lambda_0$.

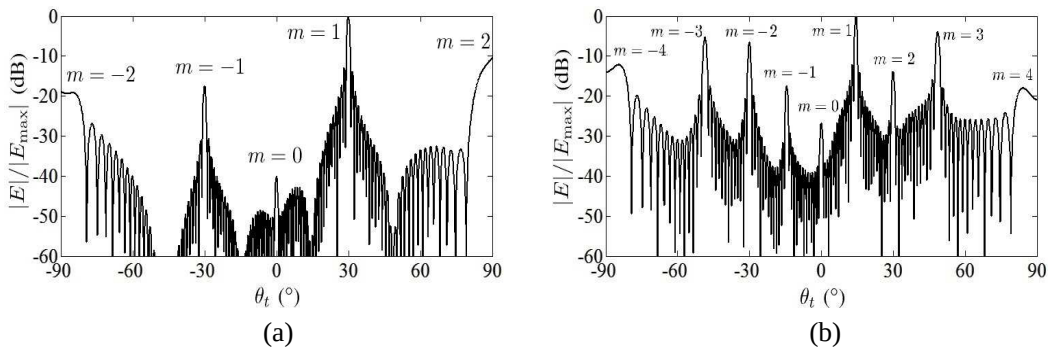

Figure 10. Far field pattern at $r = 1000\lambda_0$, with steering angle of (a) 30° and (b) 14.47°.

$d\Phi/dx = -2\pi/\Lambda$, hence (6) is reduced to

$$n_t \sin\theta_t = n_i \sin\theta_i + \frac{\lambda_0}{\Lambda} \tag{9}$$

which corresponds to the first Floquet mode predicted with (8).

In both cases shown in Figure 9, $\theta_i = 0$ and $n_i = n_t = 1$. Since the phase distribution on the Huygen's surface is a periodic function of x with period Λ, multiple Floquet modes can be excited, and the transmitted angle of the mth Floquet mode can be derived as

$$\theta_t^{(m)} = \sin^{-1}\frac{m\lambda_0}{\Lambda} \tag{10}$$

In Figure 9(a), $\Lambda = 2\lambda_0$, implying $\theta_t^{(m)} = \sin^{-1}(m/2)$. The transmitted angles of the first few Floquet modes are $\theta_t^{(0)} = 0$, $\theta_t^{(\pm1)} = \pm30^\circ$, and $\theta_t^{(\pm2)} = \pm90^\circ$, where $\theta_t^{(1)}$ is the intended steering angle. In Figure 9(b), $\Lambda = 4\lambda_0$, implying $\theta_t^{(m)} = \sin^{-1}(m/4)$. The transmitted angles of the first few Floquet modes are $\theta_t^{(0)} = 0$, $\theta_t^{(\pm1)} = \pm14.47^\circ$, $\theta_t^{(\pm2)} = \pm30^\circ$, $\theta_t^{(\pm3)} = \pm48.6^\circ$, and $\theta_t^{(\pm4)} = \pm90^\circ$; where $\theta_t^{(1)}$ is the intended steering angle. In both cases, the highest peak appears in the intended steering direction.

5. METASURFACE FOR BEAM FOCUSING

Metasurfaces have also been proposed to implement metalenses [7–10], with the phase distribution on the metasurface

$$\Phi(x,y) = \frac{2\pi}{\lambda_0}\sqrt{x^2+y^2+\ell_f^2} = \frac{2\pi}{\lambda_0}\sqrt{r^2+\ell_f^2} \tag{11}$$

where ℓ_f is the focal length of the metalens.

To focus a two-dimensional beam, the phase distribution in (11) can be rephrased as

$$\Phi(x) = 360\left[\sqrt{(x/\lambda_0)^2+(\ell_f/\lambda_0)^2} - \ell_f/\lambda_0\right] \tag{12}$$

in degrees, where the last term is added to make $\Phi(0) = 0$ for convenience.

Figures 11(a) and 11(b) show the phase distribution along x direction on the metasurface required to achieve the focal length of $\ell_f = 2\lambda_0$ and $\ell_f = 4\lambda_0$, respectively. The total width of the metasurface

Table 3. Permittivities for beam focusing with $\ell_f = 2\lambda_0$.

No.	1	2	3	4	5	6	7	8	9	10	11
ϵ_{rfout}	257	259	258	256	255	255	253	254	252	244	247
ϵ_{rfin}	259	244	250	258	258	253	254	245	246	253	248
$\lvert T\rvert$	0.8769	0.6458	0.7868	0.8678	0.8360	0.8711	0.812	0.8696	0.8757	0.8048	0.8498
$\angle T$	0.2282°	1.187°	5.231°	12.84°	22.55°	33.8°	48.57°	64.74°	84.7°	105.4°	130°
No.	12	13	14	15	16	17	18	19	20	21	22
ϵ_{rfout}	245	274	266	266	261	260	258	257	254	252	250
ϵ_{rfin}	248	271	278	274	280	273	268	257	255	249	246
$\lvert T\rvert$	0.7537	0.7965	0.8006	0.88	0.8546	0.8797	0.8724	0.8747	0.8308	0.8646	0.867
$\angle T$	154.6°	180.5°	208.8°	236.3°	267.7°	298.3°	331.5°	4.178°	38.11°	73.05°	107.7°
No.	23	24	25	26	27	28	29	30	31	32	33
ϵ_{rfout}	245	274	277	266	260	259	257	254	250	247	275
ϵ_{rfin}	249	271	268	271	275	262	253	250	249	248	271
$\lvert T\rvert$	0.8172	0.7965	0.8367	0.8105	0.8769	0.8456	0.8593	0.8724	0.8643	0.8498	0.7242
$\angle T$	144.7°	180.5°	218.3°	256.7°	293.3°	333.1°	11.9°	51.17°	90.97°	130°	169.1°

Table 4. Permittivities for beam focusing with $\ell_f = 4\lambda_0$.

No.	1	2	3	4	5	6	7	8	9	10	11
ϵ_{rfout}	259	255	256	257	257	257	256	255	256	252	251
ϵ_{rfin}	245	270	263	256	253	250	252	253	242	254	252
$\lvert T\rvert$	0.6570	0.6844	0.8345	0.8722	0.8593	0.8394	0.8747	0.8711	0.8092	0.7820	0.8069
$\measuredangle T$	0.032°	0.7405°	2.844°	6.137°	11.9°	17.42°	25.35°	33.80°	44.74°	55.45°	69.03°
No.	12	13	14	15	16	17	18	19	20	21	22
ϵ_{rfout}	253	245	249	249	246	275	277	275	269	265	261
ϵ_{rfin}	243	253	247	244	247	271	269	269	271	272	275
$\lvert T\rvert$	0.8581	0.7844	0.8676	0.7914	0.756	0.7242	0.8642	0.8705	0.85	0.8382	0.8804
$\measuredangle T$	83.04°	98.85°	113.6°	131.8°	150.9°	169.1°	189.9°	211.9°	234.6°	258°	282.1°
No.	23	24	25	26	27	28	29	30	31	32	33
ϵ_{rfout}	260	259	257	256	252	252	249	243	285	272	266
ϵ_{rfin}	269	262	259	251	254	246	247	251	267	271	274
$\lvert T\rvert$	0.8665	0.8456	0.8769	0.8721	0.782	0.8757	0.8676	0.8466	0.8311	0.8757	0.88
$\measuredangle T$	308.1°	333.1°	0.2282°	27.42°	55.45°	87.7°	113.6°	143.3°	173.5°	204.4°	236.3°

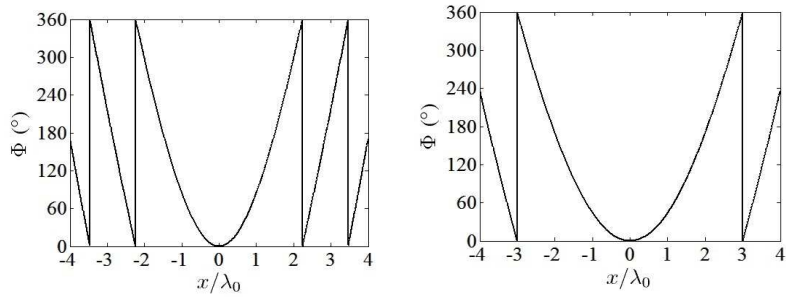

Figure 11. Required phase distribution along x direction on the metasurface, (a) $\ell_f = 2\lambda_0$ and (b) $\ell_f = 4\lambda_0$.

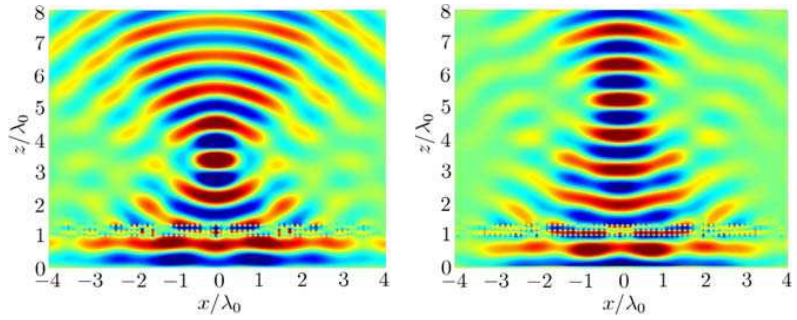

Figure 12. Distribution of E_y with (a) $\ell_f = 2\lambda_0$ and (b) $\ell_f = 4\lambda_0$.

is chosen to be $8\lambda_0$, and the incident wave is modeled as a Gaussian plane wave:

$$E_{y\text{inc}}(x,t) = -\sin(2\pi f_0 t)e^{-(x/B)^2}$$
$$H_{x\text{inc}}(x,t) = -\frac{E_{y\text{inc}}(x,t)}{\eta_0} \tag{13}$$

with $f_0 = 5.8\,\text{GHz}$ and $B = 3\lambda_0$. A total of 64 resonant units are used to realize the required phase

distribution. By symmetry with respect to x, the permittivity of 33 resonant units are chosen. Tables 3 and 4 list the required permittivities for the cases of $\ell_f = 2\lambda_0$ and $\ell_f = 4\lambda_0$, respectively.

Figures 12(a) and 12(b) show the E_y distributions with $\ell_f = 2\lambda_0$ and $\ell_f = 4\lambda_0$, respectively. The metasurface is placed at $z = \lambda_0$, and all the resonant units have the same size of $\ell = 2\,\text{mm}$ and $d = 5.5\,\text{mm}$. The incident wave is focused around $2\lambda_0$ and $4\lambda_0$, respectively, behind the metasurface.

6. CONCLUSION

The method and theories of designing tunable metasurfaces, composed of plasmonic and dielectric bricks, have been presented and simulated. Each resonant unit, composed of a ferroelectric brick with tunable permittivity and a periodical copper-wire structure with negative permittivity, is analyzed and used as building blocks to construct metasurfaces for beam steering and beam focusing, respectively. The simulation results of beam steering toward two different angles and beam focusing with two different foci have also been demonstrated.

ACKNOWLEDGMENT

This work was sponsored by the National Science Council, Taiwan, under contract NSC 102-2221-E-002-043; and the Ministry of Education, Taiwan, under Aim for Top University Project 103R3401-1.

REFERENCES

1. Kildishev, A. V., A. Boltasseva, and V. M. Shalaev, "Planar photonics with metasurfaces," *Science*, Vol. 339, No. 6125, 2013.
2. Yu, N., P. Genevet, M. A. Kats, F. Aieta, J.-P. Tetienne, F. Capasso, and Z. Gaburro, "Light propagation with phase discontinuities: Generalized laws of reflection and refraction," *Science*, Vol. 334, No. 6054, 333–337, 2011.
3. Ni, X., A. V. Kildishev, and V. M. Shalaev, "Metasurface holograms for visible light," *Nat. Commun.*, Vol. 4, Article No. 2807, 2013.
4. Farmahini-Farahani, M., J. Cheng, and H. Mosallaei, "Metasurfaces nanoantennas for light processing," *J. Opt. Soc. Am. B*, Vol. 30, No. 9, 2365–2370, 2013.
5. Zhao, Y. and A. Alú, "Manipulating light polarization with ultrathin plasmonic metasurfaces," *Phys. Rev. Lett. B*, Vol. 84, 205428, 2011.
6. Yu, N., F. Aieta, P. Genevet, M. A. Kats, Z. Gaburro, and F. Capasso, "A broadband, background-free quarter-wave plate based on plasmonic metasurfaces," *Nano Lett.*, Vol. 12, 6328–6333, 2012.
7. Aieta, F., P. Genevet, M. A. Kats, N. Yu, R. Blanchard, Z. Gaburro, and F. Capasso, "Aberration-free ultrathin flat lenses and axicons at telecom wavelengths based on plasmonic metasurfaces," *Nano Lett.*, Vol. 12, 4932–4936, 2012.
8. Lin, J., S. Wu, X. Li, C. Huang, and X. Luo, "Design and numerical analyses of ultrathin plasmonic lens for subwavelength focusing by phase discontinuities of nanoantenna arrays," *Appl. Phys. Exp.*, Vol. 6, 022004, 2013.
9. Ni, X., S. Ishii, A. V. Kildishev, and V. M. Shalaev, "Ultra-thin, planar, Babinet-inverted plasmonic metalenses," *Light Sci. Appl.*, Vol. 2, e72, 2013.
10. Jiang, X.-Y., J.-S. Ye, J.-W. He, X.-K. Wang, D. Hu, S.-F. Feng, Q. Kan, and Y. Zhang, "An ultrathin terahertz lens with axial long focal depth based on metasurfaces," *Opt. Exp.*, Vol. 21, No. 24, 30030–30038, 2013.
11. Monticone, F., N. M. Estakhri, and A. Alú, "Full control of nanoscale optical transmission with a composite metascreen," *Phys. Rev. Lett.*, Vol. 110, 203903, 2013.
12. Pors, A., M. G. Nielsen, R. L. Eriksen, and S. I. Bozhevolnyi, "Broadband focusing flat mirrors based on plasmonic gradient metasurfaces," *Nano Lett.*, Vol. 13, 829–834, 2013.
13. Pu, M., P. Chen, C. Wang, Y. Wang, Z. Zhao, C. Hu, C. Huang, and X. Luo, "Broadband anomalous reflection based on gradient low-Q meta-surface," *AIP Adv.*, Vol. 3, 052136, 2013.

14. Pors, A. and S. I. Bozhevolnyi, "Plasmonic metasurfaces for efficient phase control in reflection," *Opt. Exp.*, Vol. 21, No. 22, 27438–27451, 2013.
15. Pfeiffer, C. and A. Grbic, "Metamaterial Huygens surfaces: Tailoring wave fronts with reflectionless sheets," *Phys. Rev. Lett.*, Vol. 110, 197401, 2013.
16. Pfeiffer, C. and A. Grbic, "Cascaded metasurfaces for complete phase and polarization control," *Appl. Phys. Lett.*, Vol. 102, 231116, 2013.
17. Pfeiffer, C. and A. Grbic, "Millimeter-wave transmitarrays for wavefront and polarization control," *IEEE Trans. Microwave Theory Tech.*, Vol. 61, No. 12, 4407–4417, 2013.
18. Haus, H. A., *Waves and Fields of Optoelectronics*, Prentice-Hall, 1984.
19. Yeh, P. and C. Gu, *Optics of Liquid Crystal Displays*, Wiley, 1999.
20. Jylhä, L. and A. H. Sihvola, "Tunability of granular ferroelectric dielectric composites," *Progress In Electromagnetics Research*, Vol. 78, 189–207, 2008.
21. Kreibig, U. and M. Vollmer, *Optical Properties of Metal Clusters*, Springer, 1995.
22. Haeni, J. H., P. Irvin, W. Chang, R. Uecker, P. Reiche, Y. L. Li, et al., "Room-temperature ferroelectricity in strained $SrTiO_3$," *Nature*, Vol. 430, 758–761, 2004.
23. Jang, H. W., A. Kumar, S. Denev, M. D. Biegalski, P. Maksymovych, et al., "Ferroelectricity in strain-free $SrTiO_3$ thin films," *Phys. Rev. Lett.*, Vol. 104, 197601, 2010.
24. Pendry, J. B., A. J. Holden, W. J. Stewart, and I. Youngs, "Extremely low frequency plasmons in metallic meso structures," *Phys. Rev. Lett.*, Vol. 76, 4773–4776, 1996.
25. Wang, G., D. Moses, A. J. Heeger, H.-M. Zhang, M. Narasimhan, and R. E. Demaray, "Poly(3-hexylthiophene) field-effect transistors with high dielectric constant gate insulator," *J. Appl. Phys.*, Vol. 95, No. 1, 316–322, 2004.
26. Sheen, J., C.-Y. Li, L.-W. Ji, W.-L. Mao, W. Liu, and C.-A. Chen, "Measurements of dielectric properties of TiO_2 thin films at microwave frequencies using an extended cavity perturbation technique," *J. Mater. Sci.: Mater. Electron.*, Vol. 21, 817–821, 2010.
27. Chung, B.-K., "Dielectric constant measurement for thin material at microwave frequencies," *Progress In Electromagnetics Research*, Vol. 75, 239–252, 2007.
28. Taflove, A. and S. C. Hagness, *Computational Electrodynamics: The Finite-difference Time-domain Method*, Artech House, 2000.
29. Goodman, J. W., *Introduction to Fourier Optics*, 3rd Edition, Roberts and Company, 2005.